Title: Cobalt Doping Modification for Enhanced Methane Conversion at Low Temperature in Chemical Looping Reforming Systems

Authors: Mengqing Guo, Zhuo Cheng, Yan Liu, Lang Qin, Josh Geotze, Jonathan A. Fan, Liang-Shih Fan

PII: S0920-5861(19)30294-9
DOI: https://doi.org/10.1016/j.cattod.2019.06.016
Reference: CATTOD 12263

To appear in: *Catalysis Today*

Received date: 25 February 2019
Revised date: 17 May 2019
Accepted date: 2 June 2019

Please cite this article as: Guo M, Cheng Z, Liu Y, Qin L, Geotze J, Fan JA, Fan L-Shih, Cobalt Doping Modification for Enhanced Methane Conversion at Low Temperature in Chemical Looping Reforming Systems, *Catalysis Today* (2019), https://doi.org/10.1016/j.cattod.2019.06.016

Cobalt Doping Modification for Enhanced Methane Conversion at Low Temperature in Chemical Looping Reforming Systems

Mengqing Guo†[a], Zhuo Cheng†[a], Yan Liu[a], Lang Qin[a], Josh Geotze[a], Jonathan A. Fan[b], Liang-Shih Fan*[a]

[a] William G. Lowrie Department of Chemical and Biomolecular Engineering, The Ohio State University, 151 W. Woodruff Ave, Columbus, OH 43210, USA.
[b] Department of Electrical Engineering, Ginzton Laboratory, Spilker Engineering and Applied Sciences, Stanford University, 348 Via Pueblo Mall, Stanford, CA 94305, USA

Graphical abstract

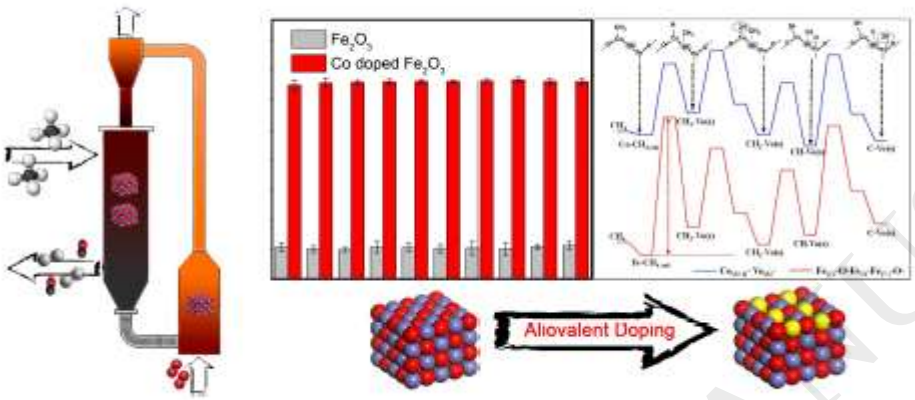

HIGHLIGHTS

- Development of iron-based oxygen carriers with aliovalent Co dopant for chemical looping methane reforming (CLR).
- Optimization of Co dopant concentration for enhancing the reactivity of iron-based oxygen carriers.
- Exploring the role of Co dopant in methane reforming over iron-based oxide oxygen carriers through density functional theory (DFT) combined experimental study.

ABSTRACT

Chemical looping reforming (CLR) is a promising strategy of methane conversion to syngas with low cost and minimal environmental impact. A major challenge for chemical looping reforming systems is the development of oxygen carriers that have high reactivity, high oxygen carrying capacity, and long-term durability. We demonstrate that the addition of a low concentration of cobalt dopant to iron-based oxygen

carriers can dramatically enhance the reactivity in CLR processes at low temperatures while maintaining the recyclability. The methane conversion increased by around 300% for Co-doped iron oxide compared to pure iron oxide oxygen carriers from 600 ^{o}C to 800 ^{o}C. It was found that 2% Co dopant concentration is optimal for methane conversion rate and cost of oxygen carriers at different temperatures. Density functional theory (DFT) simulation and thermochemistry analyses (TGA) reveal that the Co dopant has a short-range effect on the formation of oxygen vacancies. The Co-doping-induced oxygen vacancy significantly reduces energy barriers of CH_4 reforming on the surface of iron oxide oxygen carriers, leading to the reactivity enhancement. Our findings provide a pathway to lower the methane reforming temperature in chemical looping systems, while improving the syngas yield with desired oxygen carrier recyclability.

KEYWORDS

Chemical looping reforming, Syngas generation, Iron-based oxygen carrier, Cobalt doping

1. Introduction

Methane, the principal constituent of natural gas and shale gas, has been garnering attention for decades. Its relative abundance and wide distribution make it a valuable energy source from an economic point of view [1]. With its multifarious chemical properties, methane is also an excellent raw material for the production of fuels and chemicals [2]. Valuable products can be produced by methane conversion in two ways: direct conversion to C2 or higher hydrocarbons, and indirect conversion to carbon monoxide and hydrogen (syngas). Afterwards, high value chemicals can be obtained from syngas by various processes, such as Fischer-Tropsch synthesis, methanol, or dimethyl ether production [3].

Currently, syngas generation from methane can be achieved mainly via three routes: carbon dioxide (dry) reforming (CDR), steam methane reforming (SMR), and partial oxidation of methane (POM) [4][5]. However, all of the aforementioned technologies have disadvantages, such as high energy cost, high capital cost, and safety concerns [6]. Therefore, the development of technologies for efficient and cost-effective methane conversion is still an ongoing process.

Chemical looping reforming (CLR) is a promising alternative method of methane partial oxidation. CLR eliminates the need for an air separation unit, and has the potential to directly generate high-quality syngas with desirable H_2:CO ratios [7]. A CLR process involves fuel conversion taking place in two interconnected reactors: a reducer (or fuel reactor) and an oxidizer (or air reactor). In the reducer, oxygen carriers donate O atoms from their lattice for partial oxidation of methane to CO and H_2. The reduced oxygen carrier is then regenerated in the oxidizer using air with the heat thus released [8]. The reaction scheme for CLR using Fe_2O_3 as oxygen carriers is shown below:

$$\text{Reducer: } CH_4 + Fe_2O_3 \rightarrow CO + H_2 + Fe_2O_{3-x}$$

$$\text{Oxidizer: } O_2 + Fe_2O_{3-x} \rightarrow Fe_2O_3$$

Compared to the other methods for the partial oxidation of methane, CLR has advantages in lower capital cost, lower energy cost during operation, and safer operating conditions (by prohibiting direct gaseous oxygen and methane contact) [9]. Moreover, when steam is used as an oxidant, high purity hydrogen can be produced without separation processes and an adjustable syngas ratio can be implemented for downstream synthesis. Oxygen carriers are the most crucial aspect of the CLR process, since they undergo continuous redox cycles that involve reduction by methane and oxidation by air. In addition, the syngas yield depends primarily on the reactivity and selectivity of the oxygen in oxygen carriers. It is proposed that the oxygen carriers must satisfy the following requirements [10]: sufficient oxygen capacity, high reactivity and selectivity for methane to syngas (especially at low temperature), high stability during redox cycles, low cost, and low environmental impact. Enormous effort has been devoted to improving the

*Corresponding author. Email: fan.1@buckeyemail.osu.edu
The manuscript was written through contributions of all authors./ All authors has given approval to the final version of the manuscript./
†These authors contributed equally

reactivity of oxygen carriers in the past few decades. Various redox metal oxides including, nickel [11][12], tungsten [13], cerium [14][15], and iron oxides [9][16][17] show great potential. Nickel based oxygen carriers exhibit high activity for methane activation. However, the reduced nickel can promote carbon deposition, which deactivates the oxygen carriers [18]. Tungsten oxides have attracted ample attention due to their abundance, highly tuneable composition and physical stability (melting point) [19]. Nevertheless, low reactivity and bad recyclability (unstable structure of WO_3) hinder its utilization in CLR. Cerium oxides have a high selectivity, but their reactivity for methane conversion is low and their cost is too high for a commercial scale operation of CLR. In recent years, modification of perovskite materials has also been investigated to increase the selectivity and reactivity of oxygen carriers [20][21]. However, the reduced oxygen carrier's capacity and high cost of raw materials limit their application in CLR.

Compared to the oxygen carrier candidates mentioned above, iron based oxygen carriers have been demonstrated to be one of the most promising materials for CLR [9][22][23][24][25]. These oxygen carriers can sustain thousands of redox cycles without a significant decrease in reactivity and strength while operating in the CLR process [26][27]. A syngas yield of 88% with 90% syngas purity was achieved in previous work. However, the moving bed reducer was operated under iso-thermal conditions at 1000 ^{o}C. The commercial system is operated under auto-thermal conditions, which leads to a lower temperature at the reducer outlet due to the endothermic nature of the methane to syngas reaction with iron based oxygen carriers. Therefore, the reducer outlet temperature would be lower than 1000 ^{o}C when syngas yield and dry syngas purity are optimized. However, the reactivity of the iron based oxygen carriers with methane is low at temperature below 1000 ^{o}C. The catalytic doping is an efficient method for improving the activity of metal oxide materials [28]. Isovalent dopant, lanthanum, has been proven to be able to improve the methane conversion by providing highly active sites [29][30]. Aliovalent dopant, Cu, also exhibits high activity for methane conversion. The reactivity of Cu-doped oxygen carriers is higher than that of undoped iron oxide oxygen carriers universally between 700 °C and 1000 °C [31]. Despite the amount of research conducted on modifying oxygen carriers with different dopants, much work remains to be done in terms of elucidating

the relationship between the structure of oxygen carriers with dopants and the activity of the oxygen carrier, and screening more effective dopants. An understanding of the underlying reactivity enhancement mechanism is also essential to the design and development of robust oxygen carriers for CLR.

It has been reported Co dopant can significantly improve the activity of perovskite oxides for methane reforming [32]. Nevertheless, to the best of our knowledge, there is not any investigation on the effect of Co dopant on methane reforming over metal oxides [33][34]. In this work, we investigated the role of aliovalent dopant Co in CLR through density functional theory (DFT) combined experimental study. The optimal dopant concentration was determined and the formation energies of doping induced oxygen vacancies were calculated. Based on surface structure modelling and reaction barrier analysis, the mechanism of CH_4 reforming with Co doped iron based oxygen carriers was proposed. It was found that the doping induced oxygen vacancies can dramatically reduce the barriers of methane activation and dissociation, leading to the methane conversion enhancement. This work provide insights into effective oxygen carrier design and modification.

2. Experimental and Computational Details

2.1 Sample preparation

A sol gel method was applied in the fabrication of both non-doped and Co doped iron oxide. To prepare the sol gel solution, $Fe(NO_3)_3 \cdot 9H_2O$ (from Acros Organics, 99+%, for analysis) and $Co(NO_3)_2 \cdot 6H_2O$ (from Acros Organics, 99+%, for analysis) were dissolved stoichiometrically into 1 mol/L HNO_3 (from Fisher Scientific, 1.0 N). Anhydrous citric acid (from Fisher Scientific, 100.0% assay) was added afterwards. An NH_4OH (from Fisher Scientific, 28~30%) solution was utilized to adjust the pH of the aforementioned solutions to ~7.3. Ethanol was mixed with the whole solution by vigorous stirring to provide a molar ratio of nitrate salt: citric acid: ethanol of 1:2:2. A concentrated solution was obtained by heating at 270 ^oC for 1.5 hrs by hot plate and otherwise ambient conditions. Subsequently, to remove the organic residues, the

precursors were heated in a furnace with ambient air at 600 ºC for 3 hrs, with 1 ºC/min heating ramp rate and 6 ºC/min cooling ramp rate. The next process was a 2 hr-calcination at 1100 ºC, using a 2 ºC/min heating ramp rate and 6 ºC/min cooling ramp rate. The samples were eventually transferred to a small crucible to conduct a 4 hour-calcination at 1260 ºC with 2 ºC/min heating and cooling ramp rates.

2.2 Characterization

The fabricated samples were characterized using a Rigaku SmartLab X-ray Diffractometer (XRD) with eliminated fluorescence. The analysis and identification of all XRD spectra was accomplished with PDXL software and the JCPDF database. During the instrument characterization, scans were conducted from 20-80 degrees, at a rate of 1 degree per minute with accelerating voltage and filament current of 40 kV and 44 mA, respectively. The images of the samples were examined by a scanning electron microscope (SEM) with a 10 kV and 0.17 nA electron beam. Secondary electron images were obtained with a working distance of 4.1 mm. The characterization was supplemented with X-ray photoelectron (XPS) spectra, which were collected at room temperature using a Kratos Axis Ultra DLD spectrometer. Mg Kα monochromatic X-ray radiation (1253.8 eV) was utilized to ensure the optimal peak intensity of Co. Binding energy (B.E.) values were referenced to the standard C 1s binding energy of 284.8 eV. The acquired data was processed with Shirley-type background and Lorentzian-Gaussian combination and analysed by CasaXPS program.

2.3 Thermogravimetric Analysis (TGA) test operation

The prepared 15 mg sample was mounted in an alumina crucible and pre-treated at 800 ºC for 5 reduction-oxidation activation cycles. Afterwards, 10 continuous reduction-oxidation cycles were conducted at 600, 700, and 800 ºC using a Setaram SETSYS Evolution Thermogravimetric Analyzer. A 50 mL/min N_2 and 100 mL/min Helium mixture was utilized as the carrier gas for both cases. The reduction process was performed using 25% CH_4 (50 mL/min) balanced by inert gas for 5 min, while the oxidation process used 25% air (50 mL/min) balanced with inert gas for 5 min. A 10 min flushing step was also

included using the same flow rate of inert gas to prohibit the mixing of oxygen and CH_4. The definition of oxygen carrier reduction and oxidation conversion was:

$$\mathrm{Xr} = \frac{wi - wt}{wo} \times 100\%$$

where Xr is the conversion of oxygen carriers during a reduction process, wi is the initial weight (mg) of oxygen carriers in TGA, wt stands for the weight of oxygen carriers after 5 min reduction, and wo represents the weight of available oxygen in the initial state of oxygen carriers. The definition of oxidation conversion was:

$$\mathrm{Xo} = \frac{wf - wt}{wo} \times 100\%$$

where Xo is the conversion of oxygen carriers during a oxidation process, wf is the final weight of oxygen carriers after oxidation regeneration, wt stands for the weight of oxygen carriers before oxidation regeneration (since redox cycles were operated, wt is the same for one redox cycle), and wo represents the initial weight of oxygen in the oxygen carriers.

2.4 Density Functional Theory (DFT) Calculations

The first-principle calculations were performed within the framework of density functional theory (DFT), using the Vienna Ab Initio Simulation Package (VASP) [35][36][37]. The generalized gradient approximation (GGA) of Perdew, Burke and Ernzerhof [38] was used to represent the exchange-correlation energy. The projector-augmented wave (PAW) method, with a 400 eV energy cutoff, was used to describe the wave functions of the atomic cores. The tetrahedron method with Blöchl corrections was used to set the partial occupancies for the orbitals. The 8×8×1 Monkhorst-Pack k-point mesh was used for surface calculations to give results that were converged within 1×10^{-5} eV, using the conjugate gradient method. To accurately describe the strongly correlated nature of the Fe 3d electrons, the on-site coulomb repulsion of the exchange–correlation energy was treated with the GGA + U approach. We employed the effective U = 4 eV value which yielded bulk hematite properties that agreed well with density of states by experimental IPS spectra [39]. To study the effect of incorporating Co, a single Fe atom was replaced by a

Co atom in hexagonal unit cells of 120 (2×2×1) atoms. The Co/Fe ratio corresponds to 1/48, thus mimicking 2% Co concentration.

The oxygen vacancy formation energies were calculated based on the following expression:

$$E_f = E_{tot} - E_V - \frac{1}{2}E_{O_2}$$

where E_{tot} is the total energy of the stoichiometric surface, E_V is the total energy of the reduced surface with one oxygen vacancy, and E_{O_2} is the total energy of the optimized gas phase O_2. The adsorption energies of CHx (x=0−3) radicals on Fe_2O_3 (001) surface and 2% Co doped Fe_2O_3 (001) surface were calculated using the expression as below:

$$E_{ad} = E_{CHx} + E_{surf} - E_{(CHx+surf)}$$

where E_{CHx} is the energy of the optimized gas phase geometry of CHx, E_{surf} is the total energy of the respective surface, and $E_{(CHx+surf)}$ is the total energy of the slab with adsorbed CHx. Based on this definition, a greater E_{ad} corresponds to a more stable configuration.

For CH_4 activation barrier calculations, the climbing-image nudged elastic band (CI-NEB) method was used [40][41]. This method enabled the stationary points to be mapped out along the minimum energy paths and identify transition states for each of the diffusion processes. Because these paths were directed by force projection, the energy was not necessarily consistent with the force being optimized; thus, the force-based optimizer was chosen to ensure the convergence of the nudged elastic band algorithm. A modified Brønsted−Evans−Polanyi relationship was applied to correct the activation energies at different temperatures [42].

4. Results and Discussion

The impact of the Co dopant concentration on crystal phase modification was studied by XRD. ***Figure 1*** shows the XRD patterns of rhombohedral Fe_2O_3 and Co doped with various concentrations. No other phases were detected in 0.5% and 1% Co-doped Fe_2O_3 samples, indicating homogenous mixing and completion of the sol gel method. The impurity spinel phase $CoFe_2O_4$ was present in both 2% Co doped

Fe_2O_3 and 5% Co-doped Fe_2O_3 samples as indicated by the purple star in ***Figure 1***. Therefore, Co doped Fe_2O_3 oxygen carriers have dopant saturation concentrations, above which the spinel phase will form in the oxygen carrier. From the XRD patterns shown in ***Figure 1***, it can be seen that when the concentration of Co dopant is higher than 2%, the substitution of Co atoms for Fe atoms in Fe_2O_3 lattice is not applicable and a mixed metal oxide, $CoFe_2O_4/Fe_2O_3$, is formed instead. $CoFe_2O_4$ will damage the particle phase integrity, resulting in poor recyclability and weak strength of iron based oxygen carriers.

The surface modification of Fe_2O_3 by Co dopant was characterized by SEM and XPS. SEM images in ***Figure 2b, d, e, and f*** show that Co-doped Fe_2O_3 with various doping concentrations have similar average grain sizes, which are around 3.8 ~ 4.6 μm, as shown in **Table 1**, compared with pure Fe_2O_3 (***Figure 2*****a**) before the redox reaction. It indicates that the Co doped materials have less morphological change, which is advantages for chemical looping applications. 2% and 5% Co doped samples have some small cubic phases with average 300~500 nm grain size attached on the large grain boundaries, as shown in ***Figure 2e, f***, which could be attributed to the spinel phase ($CoFe_2O_4$) detected in XRD.

Chemical surface modifications caused by the dopant were analysed by XPS. ***Figure 3*** presents XPS spectra for Co $2p_{3/2}$ and O 1s in pure Fe_2O_3 as well as 0.5%, 1%, 2%, and 5% Co doped Fe_2O_3. No Co signal was detected in the pure Fe_2O_3 sample (***Figure 3a)***. The Co 2p region has observable, well-separated, satellite peak components in all Co-doped Fe_2O_3. It has been reported that the peak position of Co $2p_{3/2}$ is narrower and stronger than the Co $2p_{1/2}$ peak, and the area of the Co $2p_{3/2}$ peak is two times that of Co $2p_{1/2}$ because $2p_{3/2}$ has degeneracy of four states while $2p_{1/2}$ has only two in spin-orbit (j-j) coupling [43]. The Co $2p_{3/2}$ peak has also been associated with a satellite peak. The main Co $2p_{3/2}$ and the shake-up peak related to the Co $2p_{3/2}$ peak were still taken into account for quantification. Precise curve-fitting parameters for the Co $2p_{3/2}$ region were modified from the parameters for CoO reported by Biesinger et al [43], where the BE relationship with 5 cobalt peaks was Co_2-Co_1=2.1 eV; Co_3-Co_2=3.4 eV; Co_4-Co_3=2.6 eV; Co_5-Co_4=1.8 eV. Constrains of full width at half maximum have also been held constant. The O species ratio and Co/O ratio on the surface of Co-doped Fe_2O_3 are exhibited in **Table 2.** The ratio of Co/O is all higher than 1% from

XPS detection on the surface of Co-doped Fe_2O_3 samples, indicating successful doping modification on the surface of Fe_2O_3 for all circumstances. In addition, the XPS O 1s spectra shows that there are mainly three oxygen species, lattice oxygen (Me-O) at 529.4 eV, defective oxygen (-OH) at 531.9 eV, and organic oxygen (C=O) at 533.8 eV, on the surface. As shown in **Table 2,** the ratio of defective oxide can be another indicator for methane activation ability. Unfortunately, the ratio of –OH increases from 0 to 1% Co doped Fe_2O_3 and then drops from 1% to 5% Co doped Fe_2O_3. This predicts that the reactivity enhancement between methane and oxygen carriers will diminish when increasing their doping concentrations from 0% to 5%.

Figure 4 shows the oxygen carrier conversion rates in 10 typical cycles of methane partial oxidation and air regeneration of 2% Co doped Fe_2O_3 and undoped Fe_2O_3, respectively, at 600 ^oC (***Figure 4a, b***), 700 ^oC (***Figure 4c, d***) and 800 ^oC (***Figure 4e, f***). The reduction was carried out in 25% methane balanced by inert gas and the regeneration was conducted in 25% air balanced by inert gas as well. All the experiments have been repeated multiple times and the error bars confirm the high reproducibility of the results. The TGA analysis results indicate that 2% Co doped Fe_2O_3 has dramatically increased conversion rates in oxygen carrier reduction as well as oxygen carrier regeneration relative to un-doped Fe_2O_3. The average reduction conversion rates of 2% Co doped Fe_2O_3 were 390%, 526%, and 424% higher than that of un-doped Fe_2O_3 at 600 ^oC, 700 ^oC, and 800 ^oC, respectively, as shown in ***Figure 4a, c, e***. The average oxidation conversion rates of 2% Co doped Fe_2O_3 were 393%, 487%, and 435% higher than that of un-doped Fe_2O_3, at the same temperatures, as shown in ***Figure 4b, d, f***. The high recyclability of the oxygen carriers is also displayed in ***Figure 4***.

In addition, we studied the reactivity enhancement of Co dopant modifications with various concentrations in a wide range of operating temperatures from 600 ^oC to 800 ^oC, as shown in ***Figure 5***. All the experiments have been repeated several times and the error bars confirm the high reproducibility of the results. Larger variability at 800 ^oC is due to the activation period of methane activation with oxygen carriers. A similar trend can be seen for oxygen carrier reduction compared and oxygen carrier oxidation.

At 600 °C, the reduction conversion rates of 0.5%, 1%, 2%, and 5% Co doped Fe_2O_3 were 244%, 310%, 390%, and 423% higher than that of un-doped Fe_2O_3, respectively. At 700 °C, the reduction conversion rates of 0.5%, 1%, 2%, and 5% Co doped Fe_2O_3 were 334%, 439%, 526%, and 494% higher than that of un-doped Fe_2O_3, respectively. Meanwhile, at 800 °C, the reduction conversion rates of 0.5%, 1%, 2%, and 5% Co doped Fe_2O_3 were 222%, 363%, 424%, and 463% higher than that of un-doped Fe_2O_3, respectively. The reduction conversion rates of Co-doped Fe_2O_3 improve when the dopant concentration is increased from 0.5% to 2% in almost all circumstances. However, the enhancement of reduction conversion rates slowdown from 2% to 5% Co-doped Fe_2O_3, where a large amount of impurity spinel phase was found in XRD. Therefore, the impurity spinel phases, such as $CoFe_2O_4$, would not help to improve the conversion rates of oxygen carriers at these temperatures.

The surface oxygen species, characterized by XPS, also influence the oxygen carriers' reactivity performance. The defective oxygen, one of the oxygen species, shown in third column of **Table 2**, proved to be effective for methane oxidation and an indicator of oxygen vacancy formation on the surface. The ratios of defective oxygen in all Co-doped Fe_2O_3 samples are higher than un-doped Fe_2O_3, indicating that Co doping facilitates the oxygen vacancy formation on the surface of Fe_2O_3. However, the ratio of –OH increases for 0 to 1% Co-doped Fe_2O_3 and then drops for 1% to 5% Co-doped Fe_2O_3 samples, which explains the diminished enhancement of reduction conversion rates from 2% to 5% Co-doped Fe_2O_3 as shown in **Table 2**.

To gain mechanistic insight into the role of 2% Co doping in the reactivity enhancement of Fe_2O_3 oxygen carriers, we investigated CH_4 adsorption and dissociation on Fe_2O_3 (001) surface models with and without Co dopant using DFT+U calculations. The use of periodic models eliminates edge effects and allows for a more accurate description of surface relaxation. Depending on the cleavage position and the ordering of iron and oxygen atoms, three possible terminates can be built: $Fe_{(II)}$-O-$Fe_{(I)}$-$Fe_{(II)}$-O-, O-$Fe_{(I)}$-$Fe_{(II)}$-O-$Fe_{(I)}$- and $Fe_{(I)}$-$Fe_{(II)}$-O-$Fe_{(I)}$-$Fe_{(II)}$- as shown ***Figure 6a***. It was found that the free energy of the $Fe_{(II)}$-O-$Fe_{(I)}$-$Fe_{(II)}$-O- terminated surface is 1.22 J/m^2, which is lower than the free energy of the O-$Fe_{(I)}$-$Fe_{(II)}$-O-$Fe_{(I)}$-

terminated surface (2.05 J/m^2) and the $Fe_{(I)}$-$Fe_{(II)}$-O-$Fe_{(I)}$-$Fe_{(II)}$- terminated surface (4.03 J/m^2). Therefore, substitutions were made at the slab with the $Fe_{(II)}$-O-$Fe_{(I)}$-$Fe_{(II)}$-O- termination as shown in ***Figure 6b***. Using the first oxygen layer as the reference layer s, we replaced $Fe_{(II)}$ at the s+1 layer with one Co atom to build the doping system, $Co_{(s+1)}$-O-$Fe_{(I)}$-$Fe_{(II)}$-O-. Then one Co atom was used to replace $Fe_{(I)}$ at the s-1 layer to build the $Fe_{(II)}$-O-$Co_{(s-1)}$-$Fe_{(II)}$-O- system, or $Fe_{(II)}$ at the s-2 layer to build the $Fe_{(II)}$-O-$Fe_{(I)}$-$Co_{(s-2)}$-O- system. The surface free energy of the $Co_{(s+1)}$-O-$Fe_{(I)}$-$Fe_{(II)}$-O- system is 1.350 J/m^2, while the surface free energy of the $Fe_{(II)}$-O-$Co_{(s-1)}$-$Fe_{(II)}$-O- and $Fe_{(II)}$-O-$Fe_{(I)}$-$Co_{(s-2)}$-O- systems are 1.357 J/m^2 and 1.355 J/m^2, respectively. Similarly, we replaced an Fe atom in s-4 and s-5 layer with one Co atom, and found the surface free energies of $Fe_{(II)}$-O-$Co_{(s-4)}$-$Fe_{(II)}$-O-, and $Fe_{(II)}$-O-$Fe_{(I)}$-$Co_{(s-5)}$-O- systems were 1.353 J/m^2 and 1.356 J/m^2, respectively. This indicates that the substitution may occur on the surface or subsurface, which agrees with the experimental finding that Co dopant atoms do not have a tendency to accumulate at the surface.

For the $Co_{(s+1)}$-O-$Fe_{(I)}$-$Fe_{(II)}$-O- terminated surface, the doping effect on the oxygen vacancy formation was examined. Three defective configurations were considered: (i) the slab with one oxygen vacancy at the outmost layer adjacent to the Co dopant, labeled as $Co_{(s+1)}$-$V_{O(s)}$-, (ii) the slab with one oxygen vacancy at the subsurface close to the Co dopant labeled as $Co_{(s+1)}$-$V_{O(s-3)}$-, and (iii) the slab with one oxygen vacancy away from the dopant labeled as $Co_{(s+1)}$••• $V_{O(s)}$- (***Figure 6b***). It was found the formation energy of oxygen vacancy $V_{O(s)}$ in $Co_{(s+1)}$-$V_{O(s)}$- is 181.82 kJ/mol, which is 76.74 kJ/mol lower than that on the Fe_2O_3 surface without Co dopant. For $Co_{(s+1)}$-$V_{O(s-3)}$-, the formation energy of the oxygen vacancy $V_{O(s-3)}$ is 29.56 kJ/mol lower than the formation energy of $V_{O(s-3)}$ in the undoped surface. The oxygen vacancy $V_{O(s)}$ in $Co_{(s+1)}$•••$V_{O(s)}$- is also easier to form compared to that in the undoped surface due to a lower oxygen vacancy formation energy. This indicates that 2% concentration of Co dopant can facilitate the diffusion and removal of lattice oxygen atoms by reducing the formation energy of oxygen vacancy, which agrees with XPS results.

Previously, it was found that oxygen vacancies play an important role in CH_4 partial oxidation on a Fe_2O_3 surface [44]. Here we investigated the effect of Co doping induced oxygen vacancy on CH_4 decomposition. To determine the reaction pathway, we use a three-step approach within the framework of

DFT: (1) all possible H and CH_x adsorption sites on the Co-doped surface were examined, (2) all possible reaction paths to the intermediates and products were calculated, and the lowest barrier reaction channels were chosen as the means to reach the next intermediates, and thus the competing paths with higher reaction barriers are not investigated further, and (3) the previous two steps are repeated in succession until CH_4 is fully decomposed to one carbon atom and four hydrogen atoms . Based on this approach, the CH_4 decomposition energy profile was mapped out as shown in ***Figure 7***. TS1 denotes the transition state of CH_4 dissociation into CH_3 and H occurring on the undoped Fe_2O_3 (001) surface while TS1' represents the transition state of CH_4 initial dissociation on the 2% Co-doped Fe_2O_3 (001) surface. At the transition state TS1', the C–H bond is elongated to 1.895 Å and the distance between C and Co atom is reduced to 1.962 Å. As a result of the C–H cleavage, H binds to the nearest surface lattice O atom to form a hydroxyl species with a O–H bond of 0.955 Å. Meanwhile, the CH_3 radical moves towards the oxygen vacancy site. The barrier of this step is 85.2 kJ/mol, which is 68.3 kJ/mol lower than that of CH_4 dissociation on the undoped Fe_2O_3 (001) surface. The CH_3 radical adsorbed on Co-doped Fe_2O_3 (001) surface further dissociates to one CH_2 radical and one H atom. At the transition state TS2' of this step, the CH_2 radical remains at the oxygen vacancy site while the decomposed H atom moves towards another surface lattice O site, leading to a relatively low barrier of 80.1 kJ/mol, It indicates Co induced oxygen vacancy $V_{O(s)}$ significantly promotes CH_4 and CH_3 activation. Similarly, it was found that $V_{O(s)}$ also facilitates CH_2 and CH radical dissociation by reducing their activation barriers as shown in ***Figure 7***.

. It is worth noting that if two H atoms at two neighboring O sites of the Fe_2O_3 (001) surface directly approach each other to form H_2 (denoted as H-O path), it needs to overcome a high energy barrier of 247.1 kJ/mol due to the strong O–H bonds and the lack of active sites. This process is highly endothermic with a reaction energy of 72.3 kJ/mol. Thus, H_2 formation via binding two H atom from hydroxyl groups on the surface is both kinetically and thermochemically unfavorable. Alternatively, if one H atom migrates from the O site to the Fe site and then binds to another H atom at the O site (denoted as H-O/H-Fe path), the H_2 formation barrier can be dramatically reduced to 79.1 kJ/mol. The barriers of H migration from the O site

to the Fe site on the Fe_2O_3 (001) surface and Co-doped Fe_2O_3 (001) surface are 124.5 kJ/mol and 95.7 kJ/mol, respectively, as shown in ***Figure 8***. This result also clearly indicates Co doping favors the H_2 production.

When the oxygen carrier Fe_2O_3 is gradually reduced in CLR, Fe_3O_4 and FeO will form. Therefore, we also examined 2% Co dopant effect on the reactivity of Fe_3O_4 and FeO. 2% Co-Fe_3O_4 has a cubic inverse spinel structure with a lattice constant of 8.389 Å (8.396 Å for Fe_3O_4). The O anions form a close-packed face-centered cubic (FCC) structure with Fe^{2+} and Fe^{3+} ions located in the interstitial sites. Based on this model, we calculated the CH_4 activation barrier and found it was 59.68 kJ/mol lower than that on undoped Fe_3O_4. These results confirm that Co dopants can significantly enhance the catalytic activity of iron oxide for CH_4 conversion, which has been observed experimentally.

5. Conclusion

The low concentrations of aliovalent Co dopant can dramatically increase the reactivity of iron-based oxygen carriers for CLR while maintaining their recyclability. TGA experiments show that 2% Co dopant concentration is optimal for methane conversion rate and cost of oxygen carriers. The conversion rate of 2% Co-doped iron oxide increased by 390%, 526%, and 424% at 600 ^oC, 700 ^oC, and 800 ^oC in CLR, respectively, relative to non-doped iron oxide, DFT calculations are performed to systematically examine the oxygen vacancies and the active sites of Co-doped Fe_2O_3 oxygen carriers, as well as CH_4 activation and dissociation on the doped surface. It was found that the Co dopant can facilitate the diffusion of adjacent lattice oxygen atoms and the formation of oxygen vacancies. The Co-doping-induced oxygen vacancy not only reduces the activation barrier of CH_4 but also significantly reduces the activation barriers of CH_x radicals, leading to the reactivity enhancement of Co-doped Fe_2O_3 oxygen carrier. On the basis of activation energy calculations, a catalytic path for CLR over the 2% Co-doped Fe_2O_3 oxygen carrier is proposed where hydrogen abstraction occurs near the induced oxygen vacancy. This reveals the relationship between the surface geometry of iron-based oxygen carriers with aliovalent dopants and the activity of the oxygen carrier, and provides a catalytic dopant screening strategy for methane conversion enhancement in CLR.

These findings will contribute to the systematic design of high performance catalytic oxygen carriers for future commercialization of CLR.

Acknowledgement

The service support provided by the Center for Electron Microscopy and the Analysis, and NanoSystem Laboratory at The Ohio State University and the computing time support provided by the Ohio Supercomputer Center are gratefully acknowledged.

References

[1] R. Khalilpour, I.A. Karimi, Energy. 40 (2012) 317–328.

[2] J.R. Rostrup-Nielsen, Catal. Rev. Sci. Eng. 46 (2004) 247–270.

[3] A. Holmen, Catal. Today. 142 (2009) 2–8.

[4] B. Christian Enger, R. Lødeng, A. Holmen, Appl. Catal. A Gen. 346 (2008) 1–27.

[5] L. Bobrova, N. Vernikovskaya, V. Sadykov, Catal. Today. 144 (2009) 185–200.

[6] K. Li, H. Wang, Y. Wei, J. Chem. 2013.

[7] L.-S. Fan, L. Zeng, S. Luo, AIChE Journal. 61(2015), No. 1.

[8] L.-S. Fan, F. Li, S. Ramkumar, Particuology. 6 (2008) 131–142.

[9] S. Luo, L. Zeng, D. Xu, M. Kathe, E. Chung, N. Deshpande, L. Qin, A. Majumder, T.-L. Hsieh, A. Tong, Z. Sun, L.-S. Fan, Energy Environ. Sci. 7 (2014) 4104–4117.

[10] J. Adanez, A. Abad, F. Garcia-Labiano, P. Gayan, L.F. De Diego, Prog. Energy Combust. Sci. 38 (2012) 215–282.

[11] J. Adánez, C. Dueso, L.F. De Diego, F. García-Labiano, P. Gayán, A. Abad, Ind. Eng. Chem. Res. 48 (2009) 2509–2518.

[12] M. Rydén, M. Johansson, A. Lyngfelt, T. Mattisson, Energy Environ. Sci. 2 (2009)

[13] T. Kodama, H. Ohtake, S. Matsumoto, A. Aoki, T. Shimizu, K. Y, Energy. 25 (2000) 411–425.

[14] K. Otsuka, Y. Wang, E. Sunada, I. Yamanaka, J. Catal. 175 (1998) 152–160.

[15] K. Otsuka, T. Ushiyama, I. Yamanaka, Chem. Lett. (1993) 1517–1520.

[16] S. Luo, L. Zeng, D. Xu, M. Kathe, E. Chung, N. Deshpande, L. Qin, A. Majumder, T. Hsieh, A. Tong, Z. Sun, L.-S. Fan, Energy Environ. Sci. 7 (2014) 4104–4117.

[17] D. Sridhar, A. Tong, H. Kim, L. Zeng, F. Li, L.-S. Fan, Energy Fuels. 26 (2012) 2292–2302.

[18] P. Gayán, C. Dueso, A. Abad, J. Adanez, L.F. de Diego, F. García-Labiano, Fuel. 88 (2009) 1016–1023.

[19] D. Zhang, S. Wang, J. Zhu, H. Li, Y. Lu, Appl. Catal. B Environ. 123 (2012) 398–404.

[20] R.-J. Li, C.-C. Yu, W.-J. Ji, S.-K. Shen, Stud. Surf. Sci. Catal. (2004).

[21] L.M. Neal, A. Shafiefarhood, F. Li, ACS Catal. 4 (2014) 3560–3569.

[22] S.G. Nadgouda, M. Guo, A. Tong, L.-S. Fan, Appl. Energy. 235 (2019) 1415–1426.

[23] L. Zeng, Z. Cheng, J. A. Fan, L-S. Fan and J. Gong, Nat. Rev. Chem., 2 (2018), 349–364

[24] J. Hu, C. Li, Q. Guo, J. Dang, Q. Zhang, D. Lee, Bioresour. Technol. 263 (2018) 273–279.

[25] Z. Cheng, L. Qin, J. A. Fan, and L-S. Fan, Engineering,4 (2018), 343-351

[26] T.L. Hsieh, D. Xu, Y. Zhang, S. Nadgouda, D. Wang, C. Chung, Y. Pottimurphy, M. Guo, Y.Y. Chen, M. Xu, P. He, L.-S. Fan, A. Tong, Appl. Energy. 230 (2018) 1660–1672.

[27] C. Chung, L. Qin, V. Shah, L.-S. Fan, Energy Environ. Sci. 11 (2017) 2318–2323.

[28] M. Yang, S. Li, Y. Wang, J.A. Herron, Y. Xu, L.F. Allard, S. Lee, J. Huang, M. Mavrikakis, M. Flytzani-Stephanopoulos, Science (80-.). 346 (2014) 1498–1501.

[29] L. Qin, Z. Cheng, M. Guo, M. Xu, J.-A. Fan, L.-S. Fan, ACS Energy Lett. 2(1) (2017) 70–74.

[30] L. Qin, M. Guo, Z. Cheng, M. Xu, Y. Liu, D. Xu, J.-A. Fan, L.-S. Fan, J. Mater. Chem. A. 5 (2017) 20153–20160.

[31] L. Qin, M. Guo, Y. Liu, Z. Cheng, J.-A. Fan, L.-S. Fan, Appl. Catal. B Environ. 235 (2018) 143–149.

[32] M.H. Khazaal, J.Z. Staniforth, Z.A. Alfatlawi, R.M. Ormerod, R.J. Darton, Energy & Fuels. 32 (2018) 12826–12832.

[33] S. Mukherjee, P. Kumar, A. Yang, P. Fennell, Chem. Eng. Sci. 130 (2015) 79–91.

[34] H.A. Alalwan, D.M. Cwiertny, V.H. Grassian, Chem. Eng. J. 319 (2017) 279–287.

[35] G. Kresse, J. Hafner, Phys. Rev. B. 47 (1993) 588.

[36] G. Kresse, Comput. Mater. Sci. 6 (1996) 15–50.

[37] G. Kresse, J. Furthmüller, Phys. Rev. B - Condens. Matter Mater. Phys. 54 (1996) 11169.

[38] J.P. Perdew, K. Burke, M. Ernzerhof, Phys. Rev. Lett. 77 (1996) 3865.

[39] V.I. Anisimov, O. Gunnarsson, Phys. Rev. B. (1991).

[40] D. Sheppard, G. Henkelman, J. Comput. Chem. 32 (2011) 1769–1771.

[41] G. Henkeleman, B. Uberuage, H. Jonsson, J. Chem. Phys. 113 (2000) 9901–9904.

[42] Z. Cheng, C.S. Lo, ACS Catal. 5 (2015) 59–72.

[43] M.C. Biesinger, B.P. Payne, A.P. Grosvenor, L.W.M. Lau, A.R. Gerson, R.S.C. Smart, Appl. Surf. Sci. 257 (2011) 2717–2730.

[44] Z. Cheng, L. Qin, M. Guo, M. Xu, J.-A. Fan, L.-S. Fan, Phys. Chem. Chem. Phys. 18 (2016) 32418–32428.

Table 1 The average grain sizes of various materials

Samples	Grain sizes (μm)
Fe_2O_3	4.04
0.5% Co-doped Fe_2O_3	4.67
1% Co-doped Fe_2O_3	3.89
2% Co-doped Fe_2O_3	3.89
5% Co-doped Fe_2O_3	4.01

Table 2 The distribution of different Co or O species in samples

Sample	O 1s lattice oxygen (%)	O 1s hydrated or defective oxygen (%)	O 1s C=O, organic oxygen (%)	Co/O (%)
Fe_2O_3	50.4	40.1	9.4	0
0.5% Co-doped Fe_2O_3	54.4	45.6	0	1.1
1% Co-doped Fe_2O_3	49.0	51.0	0	1.9
2% Co-doped Fe_2O_3	41.6	49.7	8.7	1.9
5% Co-doped Fe_2O_3	46.5	41.3	12.1	2.2

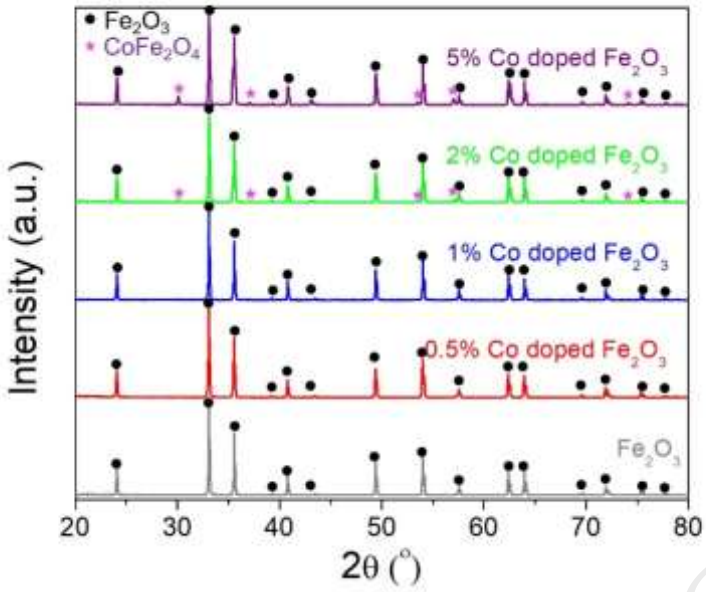

Figure 1. XRD patterns of Fe_2O_3 and Co-doped Fe_2O_3 with various dopant concentrations

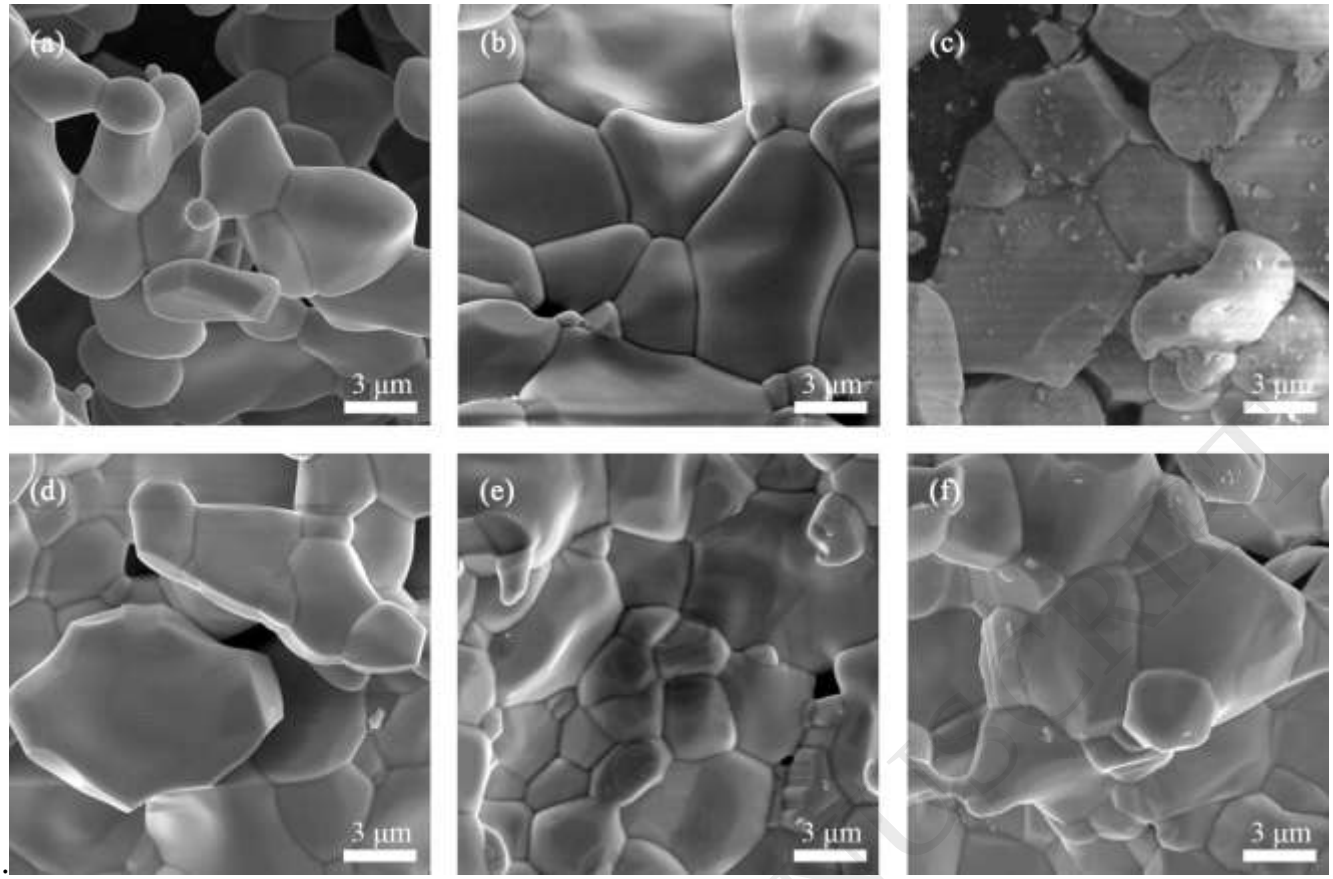

Figure 2. SEM images of of (a) Fe_2O_3, (b) 0.5% Co-doped Fe_2O_3, (c) 0.5% Co-doped Fe_2O_3 after redox cycles, and (d) 1% Co-doped Fe_2O_3, (e) 2% Co-doped Fe_2O_3, and (f) 5% Co-doped Fe_2O_3

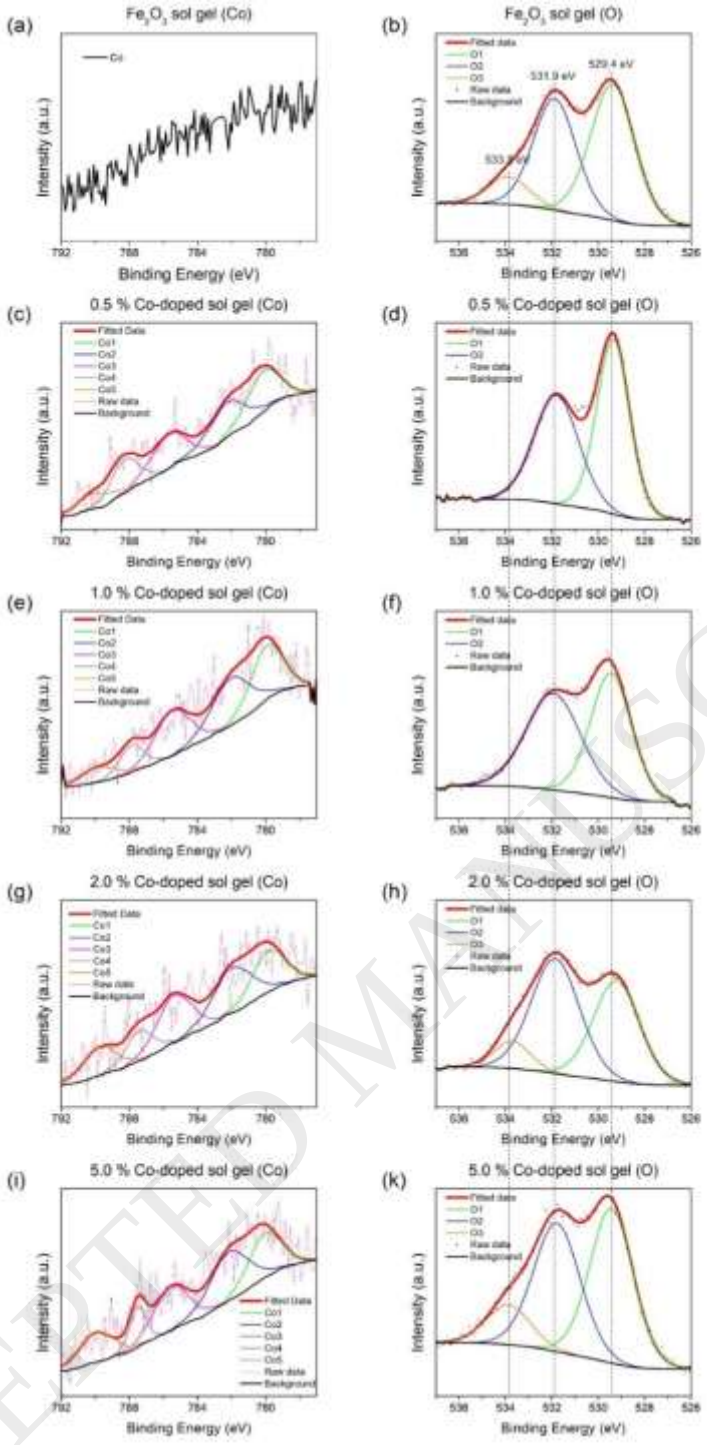

Figure 3. XPS Co $2p_{3/2}$ spectra of (a) undoped Fe_2O_3, (c) 0.5% Co-doped Fe_2O_3, (e) 1% Co-doped Fe_2O_3, (g) 2% Co-doped Fe_2O_3, (i) 5% Co-doped Fe_2O_3; O 1s spectra of (b) undoped Fe_2O_3, (d) 0.5% Co-doped Fe_2O_3, (f) 1% Co-doped Fe_2O_3, (h) 2% Co-doped Fe_2O_3, (k) 5% Co-doped Fe_2O_3

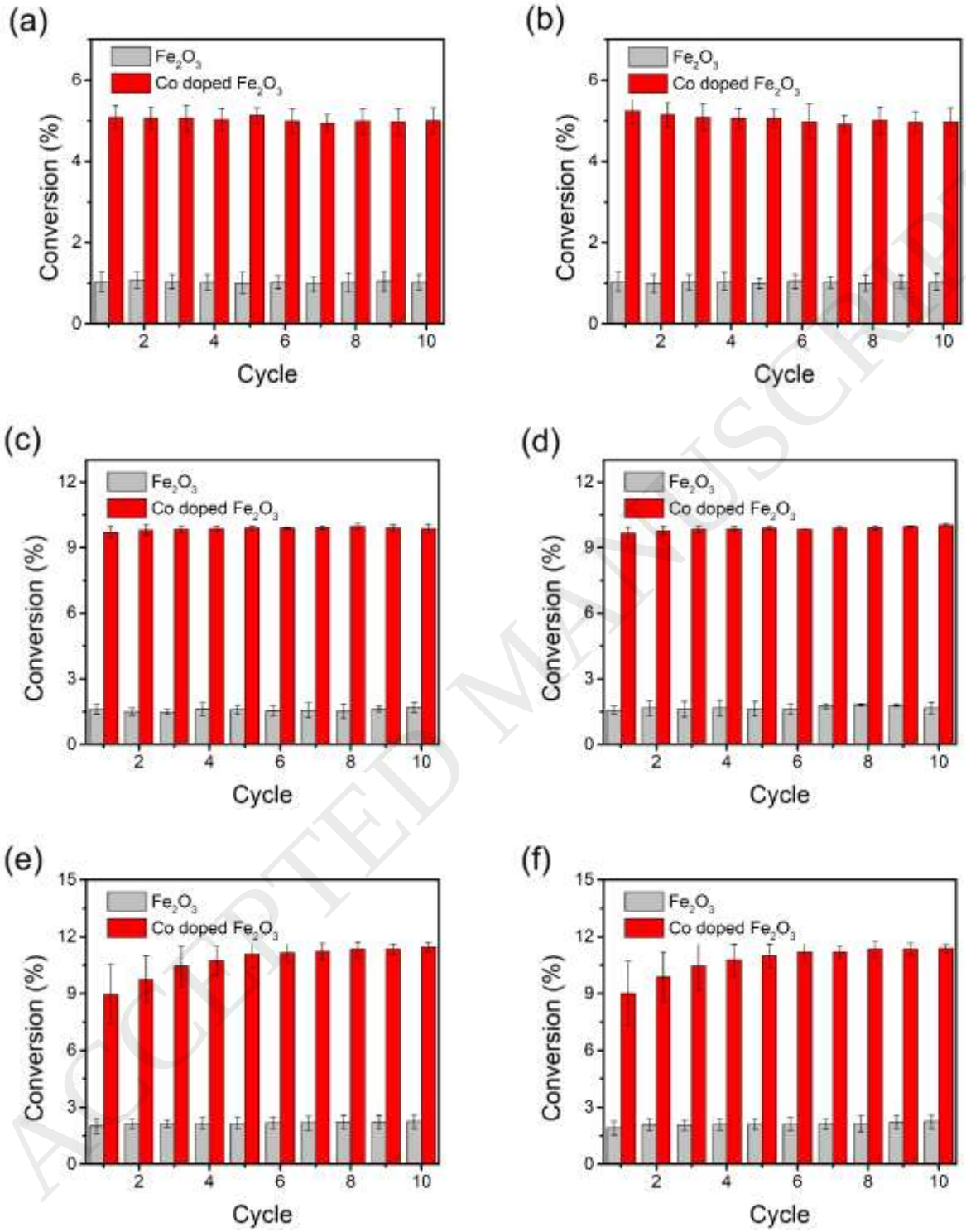

Figure 4. TGA 10 redox cycles results of Fe_2O_3 and 2% Co-doped Fe_2O_3 at 600 ^oC for (a) reduction and (b) oxidation, at 700 ^oC for (c) reduction and (d) oxidation, and at 800 ^oC for (e) reduction and (f)

oxidation, respectively.

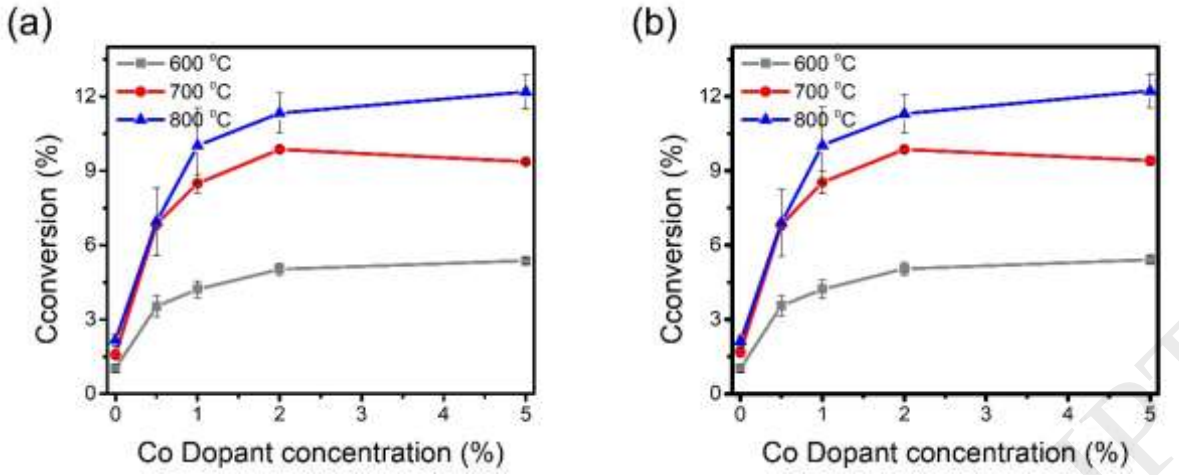

Figure 5. TGA average redox conversion results of different Co dopants concentrations at different temperatures for (a) oxygen carrier reduction and (b) oxygen carrier oxidation.

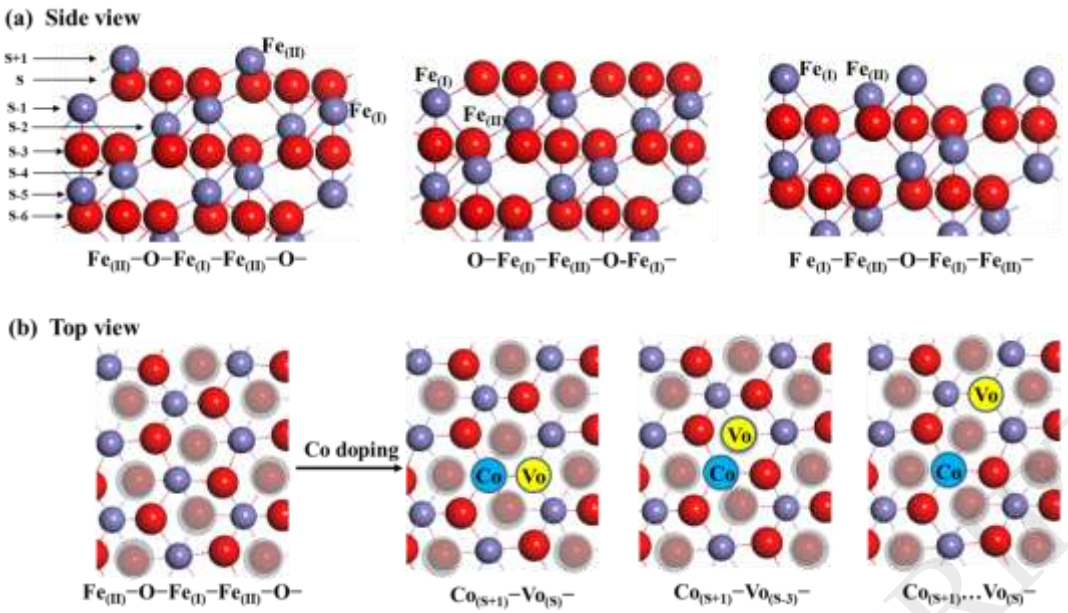

Figure 6. (a) The side view of Fe_2O_3 (001) surface with $Fe_{(II)}$-O-$Fe_{(I)}$-$Fe_{(II)}$-O-, O-$Fe_{(I)}$-$Fe_{(II)}$-O-$Fe_{(I)}$- and $Fe_{(I)}$-$Fe_{(II)}$-O-$Fe_{(I)}$-$Fe_{(II)}$- termination, (b) the top view of Co-doped Fe_2O_3 (001) surface with oxygen vacancies. The yellow balls denote oxygen vacancies, the purple balls denote Fe atoms, the red balls denote oxygen atoms and blue ball denote Co atom. The red ball with a gray circle in the top view represents the oxygen atom in the subsurface.

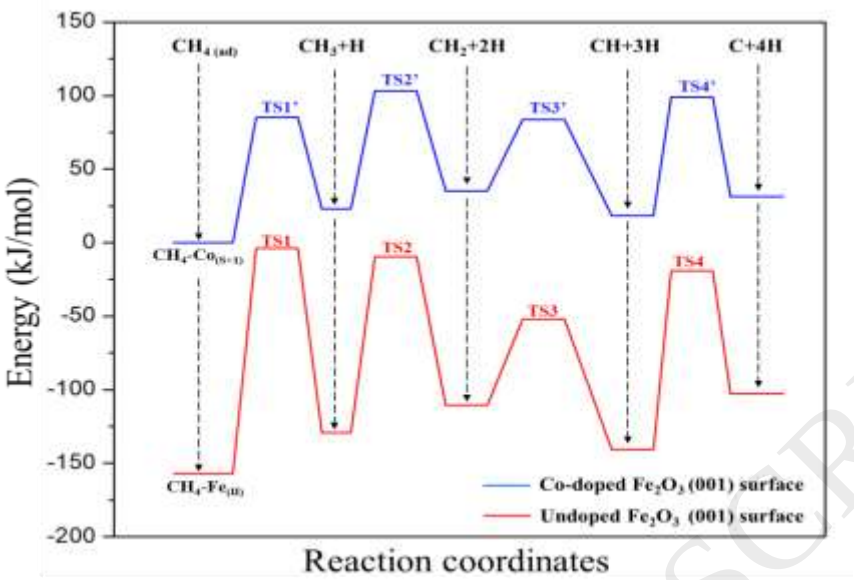

Figure 7. Energy profile for CH_4 decomposition to C+4H on the undoped Fe_2O_3 (001) surface and 2% Co-doped Fe_2O_3 (001) surface. ad denotes the adsorption.

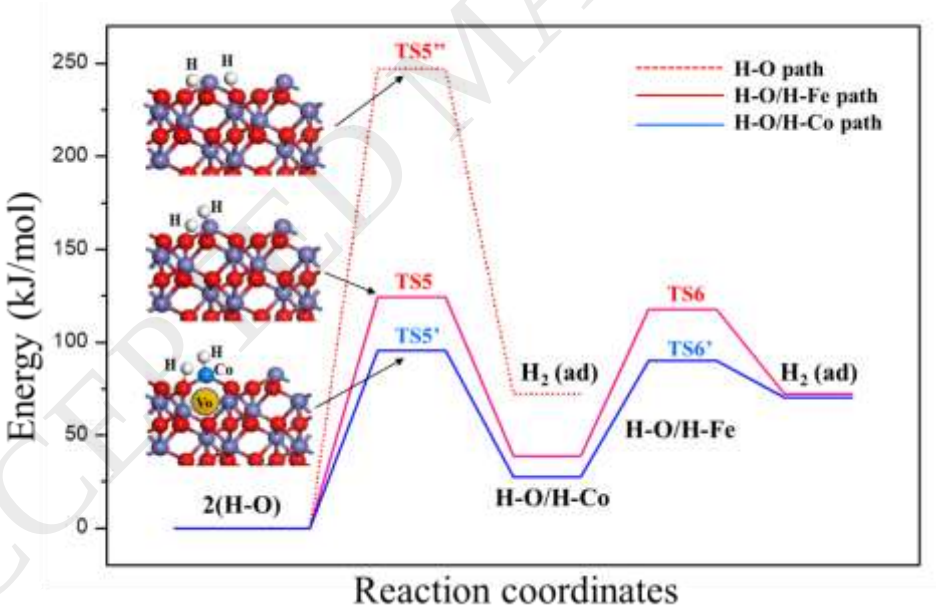

Figure 8. Energy profile for H_2 formation on the undoped Fe_2O_3 (001) surface and 2% Co-doped Fe_2O_3 (001) surface.